Final version published as: Block Copolymer Templated Synthesis of PtIr Bimetallic Nanocatalysts for the Formic Acid Oxidation Reaction, Taylor, A.K.; Perez, D.S.; Zhang, X; Pilapil, B.K.; Engelhard, M.H.; Gates, B.D.; Rider, D.A., *Journal of Materials Chemistry A*, 2017, 5 (40), 21514-21527. DOI: 10.1039/C7TA06458F

Block Copolymer Templated Synthesis of PtIr Bimetallic Nanocatalysts for the Formic Acid Oxidation Reaction

Audrey K. Taylor,[a] Diane S. Perez,[a] Xin Zhang,[c] Brandy K. Pilapil,[c] Mark H. Engelhard,[d] Byron D. Gates,[c] and David A. Rider[a,b]

Arrays of PtIr alloy nanoparticle (NP) clusters are synthesized from a method using block copolymer templates, which allows for relatively narrow NP diameter distributions (~4–13 nm) and uniform intercluster spacing (~ 60 or ~100 nm). Polystyrene-*block*-poly(4-vinylpyridine) (PS-*b*-P4VP) block copolymer micelles were used to create thin film templates of NPs with periodic pyridinium-rich domains that are capable of electrostatically loading $PtCl_6^{2-}$ and $IrCl_6^{2-}$ anion precursors for the preparation of NP arrays. The composition of PtIr NPs was specified by the ratio of metal anions in a low-pH immersion bath. Formic acid oxidation, studied by cyclic voltammetry, shows that the arrays of clusters of PtIr alloy NPs are highly active catalysts, with mass activity values on par or exceeding current industrial standard catalysts. The uniformity in the NP population in a cluster and the small diameter range established by the block copolymer template permit an estimate of the optimal Pt:Ir ratio for the direct oxidation of formic acid, where, ~10 nm $Pt_{16}Ir_{84}$ alloy NPs were the most active with a mass activity of 37 A/g.

Introduction

Direct formic acid fuel cells (DFAFCs) have demonstrated excellent power densities at ambient temperatures in miniaturized applications and, therefore, may replace current conventional batteries in future portable electronics.[1-3] Typically DFAFCs consist of two electrodes installed around a polyelectrolytic membrane (PEM) and produce electricity by passing formic acid (HCOOH) through the anode and passing oxygen (O_2) through the cathode. In idealized high-energy efficiency conditions, anodic catalysts completely oxidize HCOOH to produce protons (H^+), electrons (e^-), and carbon dioxide (CO_2). The protons pass across the PEM, whereas the e^- travel through an external circuit and back to the cathodic catalysts where they react with O_2 and the H^+ from the PEM to produce water. For nearly seven decades, a default electrocatalytic material for many of the steps in fuel cells has been monometallic platinum (Pt).[4-6] The high cost of Pt, its relatively slow kinetics towards the oxygen reduction reaction, and its susceptibility to poisoning are the major barriers to widespread commercialization of fuel cells.[7] Nanoscale and multimetallic Pt-containing catalysts have been used to overcome many of these barriers.[8] Pt-based nanoparticles (NPs) not only have a high surface area-to-volume ratio that maximizes access to surface Pt atoms, but also exhibit quantum size-dependent effects that are often greater than activities that are predicted by miniaturizing of bulk properties.[9-11]

Complementing Pt with additional metals has identified several bimetallic NP (Pt_xM_{100-x}, where M = Ru, Au, Ni, Co, Pd, etc., and subscripts indicate atomic ratios) catalysts with excellent activities for both anodic and cathodic fuel cell reactions, as well as the ability to oxidize surface adsorbed carbonaceous poisons in PEM-type fuel cells like DFAFCs.[12-16] Integration of a complementary metal in Pt NPs results in an altered geometric and/or electronic structure of the exterior NP atoms, which can tune adsorbate bonding and provide alternative catalytic pathways for electrochemical transformations. Table S1 provides a brief comparison of the catalytic activity of several bimetallic NP catalysts. The need to assess catalytic activity demonstrates the importance of specifying the stoichiometry and structure of Pt-based catalysts in the nanometer scale regime.

Bimetallic platinum-iridium (PtIr) nanocatalysts in particular have demonstrated superior activity for the oxidation of small molecule fuels, increased stability,[17] improved resistance to poisoning,[18-20] and higher rates of oxygen reduction.[21] Currently, the common route for preparing bimetallic Ir-containing nanomaterials relies on a solvothermal wet chemical reduction in media with dissolved surfactants.[22-24] The application of block copolymer templates for the preparation of bimetallic Ir-containing NPs has not yet been fully explored and represents an opportunity for discovering highly active NP catalyst arrangements.[25-29]

[a] *Department of Chemistry, Western Washington University, 516 High St., Bellingham WA 98225, USA*
[b] *Department of Engineering and Design, Western Washington University, 516 High St., Bellingham WA 98225, USA*
[c] *Department of Chemistry and 4D LABS, Simon Fraser University, 8888 University Drive, Burnaby BC V5A 1S6, Canada*
[d] *Environmental Molecular Sciences Laboratory, Pacific Northwest National Laboratory, Richland, Washington 99352, United States*

†Electronic Supplementary Information (ESI) available: [Calibration of TEM and additional STEM, BF, and HAADF images and corresponding diameter histograms for all samples are included. EDS spectra, elemental maps, and EDS composition values as well as ICP-MS data are also provided. Electrochemical characterizations are also mentioned]. See DOI: 10.1039/x0xx00000x

Lithography using solution-processable block copolymers provides a high degree of the control of the size and inter-particle spacing of NPs and NP clusters.[30] In related work, a block copolymer method for fixing PtPb NPs to a nanoporous carbon catalyst has been demonstrated, where the PtPb NP carbon composite exhibited improved anodic function in DFAFCs.[31] Conductive palladium-carbon-silica electrodes have also been prepared from a hybridized block copolymer/sol-gel route; the resulting electrodes exhibited enhanced catalytic activity where carbon-based corrosion was supressed.[32] Recently, block copolymer-patterned bimetallic and trimetallic alloy NP arrays were synthesized with precise control of size, composition, and intermetallic crystalline structure for use in controlling the vertical growth of carbon nanotubes with accelerated rates.[33]

In this work, we investigate a block copolymer templated-synthesis for the preparation of arrays of clusters of PtIr NP catalysts. Improved electrocatalytic oxidation of HCOOH by PtIr NP arrays with diameters of ~4 – 13 nm is demonstrated by our methods. We introduce: (i) the details of a block copolymer template synthesis of PtIr NP catalyst arrays from thin films of polystyrene-*block*-poly(4-vinylpyridine) (PS-*b*-P4VP) micelles (Scheme 1); (ii) a thorough characterization of the structure and composition of PtIr NP arrays; and (iii) a study of the catalytic activity by NP arrays for formic acid oxidation.

Experimental

Materials

Block ratios of ~3:1 were selected for the PS-*b*-P4VP polymers which were used as received from Polymer Source, Inc. Specifically, two polymers PS_{1392}-*b*-$P4VP_{471}$ (PDI = 1.07) and PS_{552}-*b*-$P4VP_{174}$ (PDI = 1.14) were selected as precursors for the templates in this study. Dihydrogen hexachloroplatinate hexahydrate ($H_2PtCl_6 \bullet 6H_2O$), dihydrogen hexachloroiridate hexahydrate ($H_2IrCl_6 \bullet 6H_2O$), anhydrous methanol (99.9%), trace metal grade hydrochloric acid (HCl, 34 – 37%), trace metal grade nitric acid (67 – 70%), hydrofluoric acid (HF, 49%), acetone (ACS grade), potassium permanganate ($KMnO_4$, 99.9%), and isopropyl alcohol (ACS grade) were all used as received from Fisher Scientific, Inc.(*Caution HF is highly toxic and extreme care has to be exercised while handling it.*) Sulfuric acid (H_2SO_4, 98%) and dichloromethane (99.8%) were both used as received from Macron Chemicals. Toluene (Reagent Grade, Macron Chemicals) was vacuum distilled and stored under dry N_2 prior to use. Hydrogen peroxide (H_2O_2, 30%, ACS reagent grade) was used as received from EMD Chemicals, Inc. Formic acid (HCOOH, 83%) was used as received from J.T. Baker Chemicals. Polystyrene (PS, ~200 kg/mol) was used as received from Fluka Analytical. Indium tin oxide (ITO) coated SiO_2-passivated polished float glass (8 – 12 Ω/cm^2) plates, acquired from Delta Technologies, Ltd., were used as substrates. Silicon oxide (100-nm thick) coated silicon wafer substrates were obtained from Virginia Semiconductors. All substrates were cleaned by sequential sonication in dichloromethane, ultrapure water (18 M$\Omega \bullet$cm), and isopropyl alcohol prior to use.

Synthesis of Bimetallic PtIr NP Arrays

The synthesis of PtIr NPs follows a modified protocol as outlined by Aizawa *et al*.[34] Preparation of PtIr bimetallic catalysts can be summarized by three steps: (1) the self-assembly and thin film processing of PS-*b*-P4VP diblock copolymer micelles; (2) the simultaneous absorption of $PtCl_6^{2-}$ and $IrCl_6^{2-}$ ions into the PS-*b*-P4VP film by immersion into an aqueous solution; and (3) the thermal annealing/reduction to remove the polymer and form PtIr catalyst NPs. The entire process for creating PtIr NP arrays can be carried out with standard laboratory equipment and does not require sophisticated photolithography or metal evaporation equipment or other clean-room-based fabrication techniques.

Block copolymer precursor solutions were prepared by first dissolving PS-*b*-P4VP in anhydrous toluene (4 mg/mL) at 90 ^oC under stirring for 12 h, and then allowing equilibration to room temperature before use. All substrates were subjected to an argon plasma etch for 10 min at ~0.3 Torr (Harrick Plasma, PDC 32G, 18W) directly prior to use. Thin films of PS-*b*-P4VP were prepared by spin-casting filtered polymer precursor solutions (Millipore syringe filters, PTFE, 0.45 µm pore size) directly onto substrates at 3 krpm for 60 s (Lite Laurell Spin Coater WS-400B-6NPP). Substrates coated with block copolymer films were then placed face up in methanol for 10 min causing micellar inversion as described by Chai and Buriak.[35] Substrates were dried with filtered air after removal from methanol and then submerged in 100 mM H_2SO_4 baths containing H_2PtCl_6 and H_2IrCl_6. The metal ions made up a total concentration of 10 mM in various ratios. Following metal ion loading, substrates were rinsed with ultrapure water and dried once more by filtered air. The metal ions that were loaded into the PS-*b*-P4VP template were reduced to an oxidation state of zero by annealing in a quartz tube furnace (Lindberg Blue M Mini-Mite) at 600 ^oC for 3 h with a minimum flow rate of 20 L/min of argon. Trace amounts of oxygen in the tube furnace should be avoided in order to supress the loss of Ir via the sublimation of IrO_2.[36] The atmosphere in the quartz tube was purged for 1 hr prior to annealing in order to mitigate loss of Ir content. The process for PtIr NP synthesis is depicted in Scheme 1.

General Instrumentation

Scanning force microscopy (SFM) was conducted using a Digital Instrument Nanoscope IIIa multimode instrument operated in tapping mode and equipped with conical silicon probes (Nanoscience Instruments) with resonant frequencies close to 300 kHz. Scanning transmission electron microscopy (STEM) and energy dispersive X-ray spectroscopy (EDS) were performed with a FEI Tecnai Osiris TEM system (accelerating voltage of 200 kV and a beam energy of 200 keV) equipped with an Analytical TWIN (A-TWIN) objective lens and an integrated Super-X EDS detection system. Transfer of PtIr NP arrays to a TEM grid for analysis was conducted with a polymer overcasting method. The PtIr NP arrays were created on silicon wafers bearing a 100-nm thick thermal oxide layer using the steps outlined above. The arrays were then transferred to a PS layer by spin coating (toluene solution of ~1% by wt., 3.5 krpm, 60 s). Substrates were then immersed in concentrated

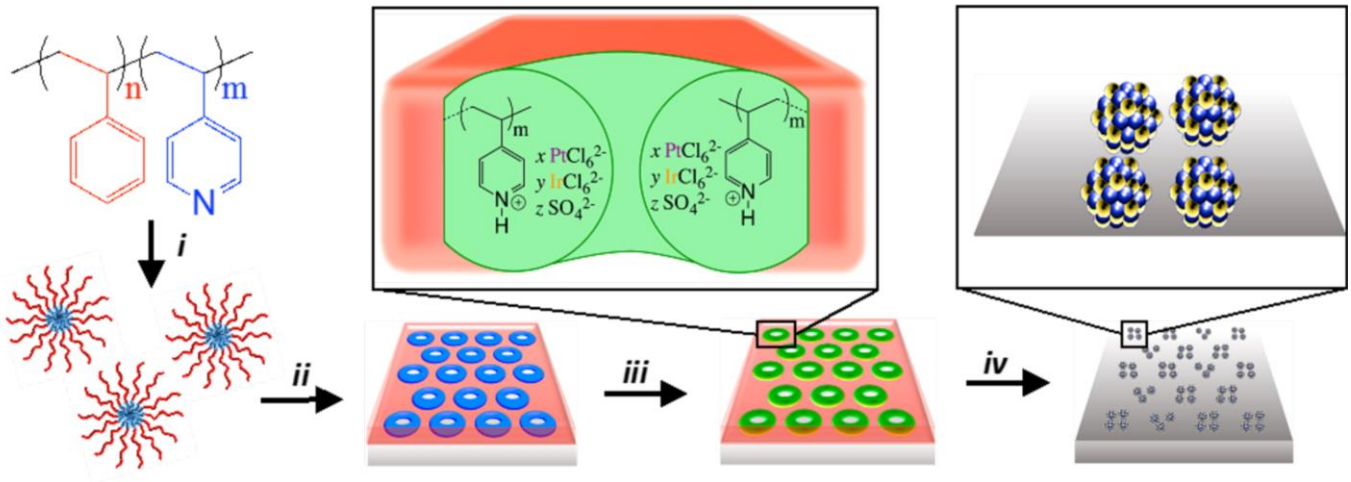

Scheme 1. General procedure for the synthesis of PtIr bimetallic catalysts using thin films of PS-*b*-P4VP micelles: (i) solution state self-assembly of PS-*b*-P4VP into spherical micelles in toluene; (ii) spin coating micelles onto an electrode substrate followed by thin film reconstruction into an array of inverted-micelles by soaking in methanol; (iii) simultaneous loading of $PtCl_6^{2-}$ and $IrCl_6^{2-}$ ions into the micellar array by immersion into a stoichiometrically tuned aqueous solution of the respective metal ions; and (iv) removal of PS-*b*-P4VP template by thermal annealing under Ar. The *x* and *y* coefficients indicate the amount of $IrCl_6^{2-}$ and $PtCl_6^{2-}$ of metal ions incorporated into a single PS-*b*-P4VP micelle domain, while the *z* coefficient refers to the incorporated sulfate ions from the 100 mM H_2SO_4 ion-loading immersion bath.

HF for ~30 s, which caused etching of the thermal oxide layer and release of the PS film containing the embedded PtIr NP arrays. TEM grids were then used to capture the floating films and rinsed with ultrapure water and stored for later analysis by STEM and EDS. This TEM transfer method has previously been shown to not significantly alter the composition of Pt-based NPs from that found on ITO electrodes.[28]

X-ray photoelectron spectroscopy (XPS) measurements were performed with a Physical Electronics Quantera Scanning X-ray Microprobe. This system used a focused monochromatic Al Kα X-ray (1486.7 eV) source for excitation. The instrument has a 32 element multichannel detection system. The X-ray beam was incident normal to the ITO-supported samples and the photoelectron detector was at 45º off-normal. High energy resolution spectra were collected using a pass-energy of 69.0 eV with a step size of 0.125 eV. For the Ag $3d_{5/2}$ line, these conditions produced a FWHM of 1.07 eV. The binding energy (BE) scale was calibrated using the Cu $2p_{3/2}$ feature at 932.62 ± 0.05 eV and Au $4f_{7/2}$ at 83.96 ± 0.05 eV. The atomic concentrations were quantified using standard sensitivity factors contained in the ULVAC-PHI, Inc. MultiPak software V9.6.1.7 dated 10/2016. Peak area intensities required for quantification were calculated after applying a Shirley background subtraction. These quantification results include the instrument transmission function, source angle, and asymmetry corrections.

Quantitative elemental analysis of PtIr NPs was conducted by inductively coupled plasma mass spectrometry (ICP-MS) on an Agilent 7500ce. An integration time of 0.1 s was applied using an on-axis octopole reaction system operated in collision mode using ultra-high purity He. All glassware used in the process was stored in a concentrated HCl bath overnight. Calibration standards were prepared by dissolving calculated amounts of H_2PtCl_6 and H_2IrCl_6 in a solution of 5% nitric acid (v/v), resulting in concentrations in the range of 0.01 – 10 ppm. The concentrated metal solution was diluted by 10-fold serial dilutions for a total of eight standards with an identical matrix composition of 5% nitric acid (v/v). PtIr catalysts mounted on ITO of known dimensions were dissolved in concentrated aqua regia (*CAUTION: Aqua regia solution is extremely corrosive and must be handled with caution*) for a minimum of 15 min (lack of conductivity from ITO substrates confirmed the full dissolution of PtIr NPs) and diluted to 5% (v/v) in sterile polycarbonate 50 mL volumetric tubes.

Electrochemical Methods

Stringent cleaning procedures were used on all glassware and samples in order to reduce the influence of organic contaminants during electrochemical measurements. The electrochemical cell and fritted glass tube for sparging were both soaked overnight in a strong oxidizing bath of aqueous 1 M H_2SO_4 and ~1 mM $KMnO_4$. The resulting residue from the glassware was removed by rinsing with piranha (*CAUTION: Piranha solution reacts violently with organics and should be handled with extreme caution*) and lastly with ultrapure water. The ITO substrates supporting PtIr nanocatalysts were cleaned with acetone using a Soxhlet extractor for a minimum of 12 h prior to electrochemical measurements.

Electrochemical characterizations were carried out on either a WaveDriver 20 Bipotentiostat or a WaveNow Potentiostat (Pine Research Instrumentation). Electrochemical measurements were obtained at ambient temperatures using a standard three-electrode electrochemical cell that consisted of a ferricyanide-corrected silver/silver chloride reference electrode (Ag/AgCl), a wire platinum counter electrode and ITO coated glass with PtIr NP catalysts as the working electrode. The geometric area of the working electrode was immediately measured after electrochemical testing using a digital caliper, which allowed for cyclic voltammetric (CV) plots to be reported in a mass specific current (A/g) when required.

Electrochemical surface area (ECSA) was evaluated by CO-stripping using a modified protocol as outlined by Jerkiewicz *et al.*[37]

High purity argon (Ar, 99.999%) was bubbled through a 0.5 M H_2SO_4 electrolyte for 30 min prior to measurements. High-purity CO was purged through the electrolyte for 5 min at a constant chemisorption potential of 0.1 V. The electrolyte was purged once more with argon for 30 min at the same potential to displace any remaining CO in the cell. Oxidative stripping voltammograms and subsequent CVs were then acquired at a scan rate of 20 mV/s.

Oxidation of HCOOH and multi-cycle testing was carried out in 0.5 M H_2SO_4 and 0.1 M HCOOH purged with argon for 30 min prior and a constant flow of argon gas was allowed to flow in and out of the headspace of the cell during electrochemical testing. A scan rate of 10 mV/s was used for 25 consecutive cycles between -0.25 and 1.30 V or until steady-state conditions were reached. The exposed catalytic area of the working electrode was immediately measured upon removal from the measurement using a digital calliper.

Results and Discussion

Arrays of PtIr NPs from Diblock Copolymer Templates

The arrays of PtIr NPs discussed in this work were synthesized from diblock copolymer templates created from self-assembled micelles of PS-*b*-P4VP.[38-40] Specifically, two size regimes for PtIr NP arrays are investigated, which are defined by two different block copolymers, namely PS_{1392}-*b*-$P4VP_{471}$ and PS_{552}-*b*-$P4VP_{174}$. The subscripts indicate the average number of repeat units for each block. A PS:P4VP block ratio of approximately 3:1 was chosen in order to achieve a spherical micelle morphology in toluene, a PS block-selective solvent.[41] In toluene, P4VP chains collapse into a micelle core that is stabilized by a highly solvated PS corona. Spin coated films from these micellar solutions yield monolayer arrays of quasihexagonally packed PS-*b*-P4VP micelles that consist of a continuous matrix of vitrified PS with embedded P4VP micelle cores. The height mode SFM images of ITO-supported films of quasihexagonally packed micelles from PS_{1392}-*b*-$P4VP_{471}$ and PS_{552}-*b*-$P4VP_{174}$ are shown in Fig. 1a and 1b. Both the molecular weight of the block copolymer and the processing conditions determine the dimensions of self-assembled features in this type of micellar film.[42] Table S2 in the Supporting Information file reports the periodicity, the average full width at half-maximum (FWHM), and height values of the micelles in both films. The higher molecular weight block copolymer, PS_{1392}-*b*-$P4VP_{471}$, creates an array of larger micelles with an approximate periodicity of 101 nm while the lower molecular weight PS_{552}-*b*-$P4VP_{174}$ creates an array of smaller micelles with an approximate periodicity of 63 nm. Similarly, the height and FWHM values for the larger block copolymer are greater than those of the smaller block copolymer.

The approach for loading aqueous metal ion precursors into the P4VP domains of the micelles requires a priming step that reconstructs the continuous PS matrix that results from spin casting. Initially, the PS acts as a barrier between aqueous ions and pyridinyl sites in the micelle cores. The PS-*b*-P4VP micelles readily undergo inversion when exposed to orthogonal solvents like alcohols.[43-46] In this reconstruction step, the P4VP domains in the micelle films become highly swollen in alcohol and increase in size by several-fold, creating large swelling forces at the P4VP/PS boundary.[47, 48] The solvent-swollen P4VP chains can, therefore, breach across any PS overlayer in order to better contact the solvent. Local fixation of P4VP chains to the surface is facilitated by the solvophobic PS matrix present in between micelles, which focuses the reconstruction to the region above the embedded P4VP cores. Solvent-swollen P4VP chains collapse back onto the films upon drying and transform a hemi-spherical micellar feature in the films (Fig. 1a and 1b) into a toroidal analogue (Fig. 1c and 1d). This methanol-triggered reconstruction step (Scheme 1, step *ii*) was found to improve the metal ion loading step and has been included in the process for defining the block copolymer templates. Each SFM image confirms that the reconstruction step has successfully positioned P4VP chains at the surface of the film, which allows for more effective interaction with aqueous phase metal ions.

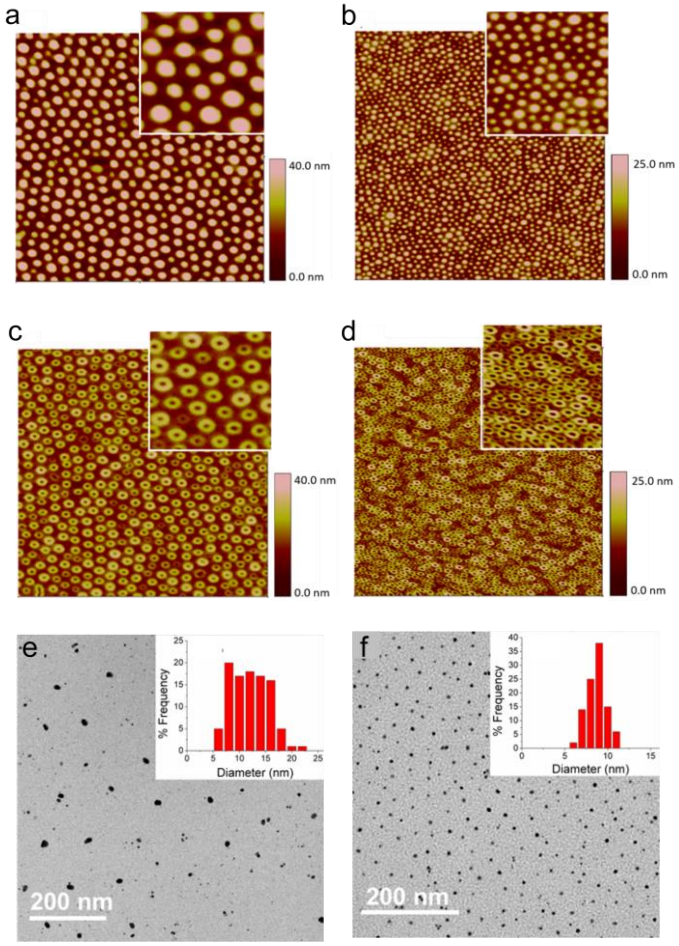

Fig. 1 SFM height mode images (2 x 2 μm²) for as cast (a) PS_{1392}-*b*-$P4VP_{471}$ and (b) PS_{552}-*b*-$P4VP_{174}$ templates created by spin-coating onto ITO. The corresponding SFM images for the inverted micelles are shown in (c) and (d). Insets images are 250 x 250 nm² and use the same height scale. Representative bright field STEM images of Pt_xIr_{100-x} NP cluster arrays created by thermoreductive annealing of (e) PS_{1392}-*b*-$P4VP_{471}$ and (f) PS_{552}-*b*-$P4VP_{174}$ templates that were loaded from a 100 mM H_2SO_4 aqueous solution of 9.0 mM H_2PtCl_6 + 1.0 mM H_2IrCl_6. The corresponding particle diameter histograms are shown as insets in (e) and (f).

The pKa of the pyridinyl residues in the P4VP core is ~ 4.5 and, therefore, these groups can be protonated at low pH values.[49, 50] The immersion baths that load NP precursors into the templates have been defined to include dissolved $PtCl_6^{2-}$ (from H_2PtCl_6) and $IrCl_6^{2-}$

anions (from H_2IrCl_6), as well as H_2SO_4 in order to access a low pH media and to convert pyridinyl groups into their cationic form. The negatively charged $IrCl_6^{2-}$ and $PtCl_6^{2-}$ are expected to mainly coordinate to cationic pyridinium groups by an electrostatic interaction.[51] A series of ten immersion baths were investigated in this work (see Supporting Information Table S3), where the immersion time was held constant for 10 min, only six of the baths are shown in Table 1. Each immersion bath is defined to include 100 mM H_2SO_4 and a total metal ion concentration of 10 mM, each differentiated by the following Pt:Ir molar ratios: 10:0, 9.75:0.25, 9.5:0.5, 9.0:1.0, 8.0:2.0, 7.5:2.5, 7.0:3.0, 5.0:5.0, 2.4:7.6, and 0:10. After recovering $PtCl_6^{2-}$- and/or $IrCl_6^{2-}$ loaded block copolymer templates, a thermoreductive annealing step [3 h, 600°C, flowing $Ar_{(g)}$] was used to remove the PS-*b*-P4VP template, reduce the metal ions, and alloy Pt and Ir into NPs (Scheme 1, step *iv*).

Samples for STEM analyses were created by transferring the PtIr NP arrays synthesized on thermal SiO_2 coated Si wafers to TEM grids. PtIr NP arrays were synthesized on the wafers, embedded in a PS homopolymer layer by spin coating, and floated off the substrate using aqueous HF and transferred to a TEM grid. While some distortion of the arrays occurs, the dimensional characteristics of the arrays of NP that are transferred to the TEM grid are generally close to those determined for the same arrays supported on ITO substrates and investigated by SFM (see Fig. S1 for representative SFM). Shown in Figure 1e-f are representative STEM bright field images of the NP arrays that are created from the PS_{1392}-*b*-$P4VP_{471}$ and PS_{552}-*b*-$P4VP_{174}$ templates prepared from the immersion bath containing a 9.0:1.0 molar ratio of Pt:Ir, respectively. A complete set of STEM bright field images for both block copolymer templates matched to each immersion bath can be found in the Supporting Information file (Fig. S2 and S3). The thermoreduction of a metal-ion-loaded P4VP domain leads to PtIr NP arrays in the form of clusters. The number of NPs per cluster found for each PS_{1392}-*b*-$P4VP_{471}$ and PS_{552}-*b*-$P4VP_{174}$ template-immersion bath combination was determined and is reported in Table 1 and Table S3. For higher Pt-content target bimetallic NPs (immersion baths with ≥ 95 mol% Pt), the PS_{1392}-*b*-$P4VP_{471}$ template leads to arrangements with ~6-7 NPs per cluster. For lower Pt-content target bimetallic NPs (immersion baths with < 95 mol% Pt), the PS_{1392}-*b*-$P4VP_{471}$ template leads to clusters of NPs with ~1-2 NPs per cluster. The use of the PS_{552}-*b*-$P4VP_{174}$ template results in analogous cluster definition. When high Pt-content is targeted for PtIr NPs, ~4-7 NPs per cluster result for this lower molecular weight template. Similarly, lower Pt-content in the PtIr NPs favours ~1-2 NPs per cluster from the same lower molecular weight template. In the high Pt-content targets, the observation of fewer NPs per cluster between templates (6-7 vs 4-7 NPs per cluster) suggests that the size of the P4VP domain in the block copolymer template specifies the number of NPs that can be isolated from a single micellar domain.

Table 1. Comparison of twelve compositionally tuned particle clusters synthesized from immersion into 100 mM H_2SO_4 with 10 mM [H_2IrCl_6 + H_2PtCl_6].

Pt : Ir molar ratio in immersion bath	NP and Cluster Parameters	PS_n-*b*-$P4VP_m$ Diblock copolymer template[a] and TEM estimated dimensions (Std. Dev.)	
		PS_{1392}-*b*-$P4VP_{471}$	PS_{552}-*b*-$P4VP_{174}$
10 : 0	NP Diameter[b]	10 ± 4 nm	6 ± 3 nm
	NPs per Cluster[c]	2 ± 1	7 ± 3
	Periodicity[d]	116 ± 7 nm	56 ± 9 nm
	Stoichiometry Estimated by XPS	$Pt_{100}Ir_0$	$Pt_{100}Ir_0$
9.5 : 0.5	NP Diameter[b]	4 ± 1 nm	6 ± 2 nm
	NPs per Cluster[c]	6 ± 3	4 ± 2
	Periodicity[d]	144 ± 19 nm	74 ± 11 nm
	Stoichiometry Estimated by XPS	$Pt_{91}Ir_9$	$Pt_{79}Ir_{21}$
8.0 : 2.0	NP Diameter[b]	13 ± 5	9 ± 1
	NPs per Cluster[c]	1.6 ± 1.0	1.8 ± 1.2
	Periodicity[d]	116 ± 14 nm	45 ± 7 nm
	Stoichiometry Estimated by XPS	$Pt_{33}Ir_{67}$	$Pt_{36}Ir_{64}$
7.0 : 3.0	NP Diameter[b]	9 ± 1	9 ± 1
	NPs per Cluster[c]	2.4 ± 1.1	1.2 ± 0.5
	Periodicity[d]	128 ± 7 nm	49 ± 8 nm
	Stoichiometry Estimated by XPS	$Pt_{18}Ir_{82}$	$Pt_{20}Ir_{80}$
5.0 : 5.0	NP Diameter[b]	11 ± 3	10 ± 1
	NPs per Cluster[c]	2.2 ± 1.3	1.2 ± 0.4
	Periodicity[d]	112 ± 15 nm	49 ± 8 nm
	Stoichiometry Estimated by XPS	$Pt_{19}Ir_{81}$	$Pt_{16}Ir_{84}$
0 : 10	NP Diameter[b]	13 ± 5 nm	10 ± 4 nm
	NPs per Cluster[c]	n/a*	n/a*
	Periodicity[d]	123 ± 13 nm	66 ± 12 nm
	Stoichiometry Estimated by XPS	Pt_0Ir_{100}	Pt_0Ir_{100}

[a] *n* and *m* represent the average number of repeat units of the PS and P4VP blocks, respectively. [b] Average of 100 particles. [c] Average of 25 clusters. [d] Average of 15 clusters. * Continuous metal phase present in nanoring formation.

Further quantification of the STEM images was conducted, and Table 1 also reports the average distance between clusters (periodicity) and NP diameter and for each template / immersion bath combination. The periodicity values were found to be close to those of the parent block copolymer micellar films (Table S2). Lastly and in general, the thermoreductive isolation of block copolymer templated PtIr NP clusters yields NPs that are between 4-13 nm in diameter. The diameter distribution histograms for PtIr NPs from the PS_{1392}-*b*-$P4VP_{471}$ and PS_{552}-*b*-$P4VP_{174}$ templates loaded with the 9.0:1.0 Pt:Ir immersion baths are reported as insets in Fig. 1e-f while all others are reported in the Supporting Information file (Fig. S2 and S3). The relatively narrow distribution in NP diameter found for all NPs from each series is a testament to the controlled synthetic conditions for NP nucleation and growth that are imparted by the block copolymer template.

The prevalence of several small NPs per cluster across the series suggests several aspects of the NP growth mechanism: (i) the high temperature thermoreductive and/or annealing step initially yields several NP nuclei per ion-loaded micelle domain; and (ii) coalescence of neighbouring NPs into larger NPs can occur but is minimized during this annealing process.[52-54] The smallest average NP diameter values were found for Pt-rich NPs created from both polymer templates loaded with immersion baths with ≥ 95 mol% Pt. Other morphological exceptions are found for the arrays of monometallic Ir NPs created from both block copolymer templates. In these cases, a single ring-like NP of Ir was created from each $IrCl_6^{2-}$ loaded P4VP domain (rather than a cluster; see Fig. S2s and S3s in the Supporting Information file). The suppression of the growth mechanism in the clusters is proposed to be linked to the oxophilicity and low mobility of monometallic Ir.[55-58] Overall, the STEM investigation confirms that the processing steps taken with the two PS-*b*-P4VP templates and immersion baths are capable of creating arrays of quasihexagonally organized clusters of PtIr NPs.

Composition and Structure of PtIr NP Arrays

A more detailed understanding of the composition and structure of the NPs created from the block copolymer template approach is derived from STEM-coupled EDS analysis. The monometallic NPs created from immersion baths containing only $PtCl_6^{2-}$ or $IrCl_6^{2-}$ anions were not investigated by STEM-EDS analysis. The Lα X-ray emission signals for Pt and Ir at 9.44 keV and 9.17 keV and the Mα X-ray emission signals at 2.05 keV and 1.98 keV were resolved in Bremsstrahlung-corrected EDS spectra for arrays of PtIr bimetallic NPs and NP clusters. These signals were used to: (i) create elemental maps; (ii) determine the Pt:Ir ratios for isolated NP clusters; and (iii) analyze the same for large regions of clusters (areas of 0.12 μm^2 and 0.056 μm^2 for PS_{1392}-*b*-$P4VP_{471}$ and PS_{552}-*b*-$P4VP_{174}$ templated arrays, respectively). Bremsstrahlung-corrected EDS spectra are presented in the Supporting Information (Fig. S4, S5, and S6). Shown in Fig. 2a-b are the representative high angle annular dark field (HAADF) images for arrays of clusters of PtIr NPs created from thePS_{1392}-*b*-$P4VP_{471}$ and PS_{552}-*b*-$P4VP_{174}$ templates loaded using 100 mM H_2SO_4 aqueous solutions of 8.0 mM H_2PtCl_6 + 2.0 mM H_2IrCl_6. The corresponding elemental maps for Pt and Ir are shown in Fig. 2c-d and Fig. 2e-f, respectively. The Pt and Ir elemental maps from the PS_{1392}-*b*-$P4VP_{471}$ (Fig. 2c and 2e) show that the arrangement of Pt and Ir signal intensities correspond with one another and are also associated with the arrangement of the NPs found in the corresponding HAADF image (Fig. 2a). The Pt:Ir ratio found for a large area of the array was 59:41, while the ratio for three selected clusters within this region had a range of ratios from 44:56 to 47:53. The difference in the EDS-determined Pt:Ir ratio between individual NP clusters and large areas of the array can be attributed to the presence of diffuse Pt and Ir for the more comprehensive area analyses. The Pt:Ir ratio is consistent between individual NPs within an array, which confirms that the composition of PtIr NP cluster arrays is quite uniform. The

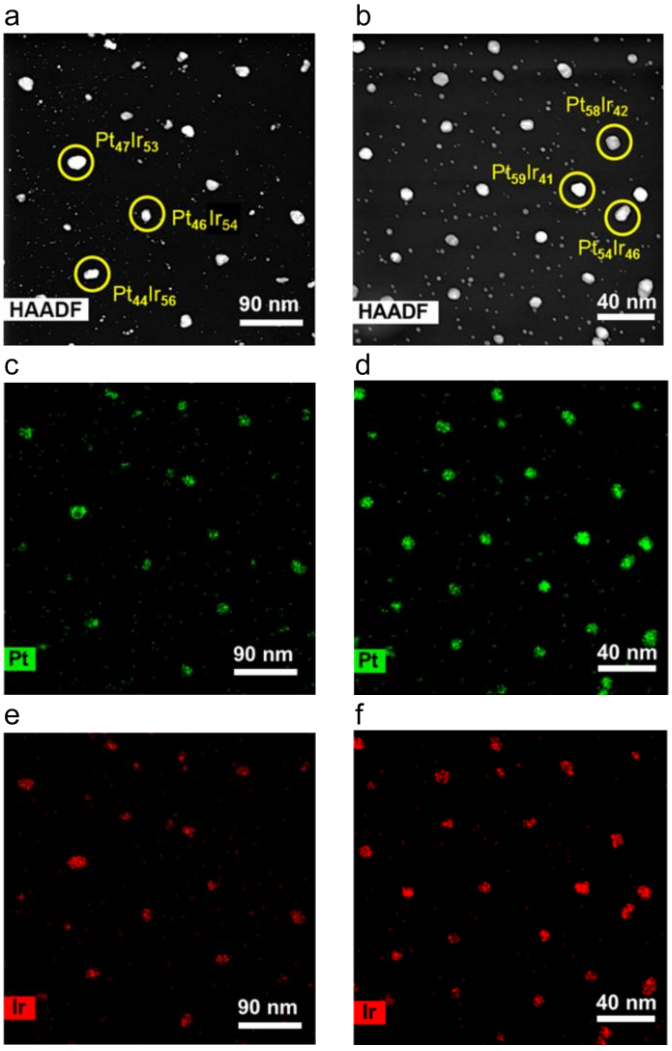

Fig. 2 HAADF STEM images of PtIr NP clusters created by the thermoreduction of (a) PS_{1392}-*b*-$P4VP_{471}$ and (b) PS_{552}-*b*-$P4VP_{174}$ templates that were loaded with $PtCl_6^{2-}$ to $IrCl_6^{2-}$ from 100 mM H_2SO_4 aqueous solutions of 8.0 mM H_2PtCl_6 + 2.0 mM H_2IrCl_6. For (a), the corresponding Lα X-ray emission Pt and Ir elemental maps are depicted in (c) and (e) while those for (b) are depicted in (d) and (f), respectively. The circled regions indicate the EDS-estimated composition of the PtIr NPs.

conclusions for the Pt and Ir elemental maps from the PS_{552}-*b*-$P4VP_{174}$ template are largely similar. The isolated NPs in Figure 2b have a Pt:Ir range of 54:46 to 59:41, while the overall ratio within this area of interest was 66:33. A solid–solution alloy structure is therefore suggested for the NPs.

Similar structural conclusions are found in the STEM-EDS analysis of the arrays of PtIr NPs created from the PS_{1392}-*b*-$P4VP_{471}$ and PS_{552}-*b*-$P4VP_{174}$ templates loaded with the other immersion baths (see Supporting Information Figures S4, S5, and S6). Pt and Ir were found to be commonly located and matched in position to the NPs identified by HAADF-STEM.

The complex nanostructures in the PtIr NPs found by HAADF STEM analysis were further investigated by high-resolution transmission electron microscopy (HRTEM). Shown in the Supporting Information file (Fig. S7, S8, and S9) are the HRTEM analyses and corresponding Fast-Fourier Transform (FFT) images for individual NPs isolated from arrays of clusters of PtIr NPs prepared using the PS_{1392}-*b*-$P4VP_{471}$ and PS_{552}-*b*-$P4VP_{174}$ templates loaded with the 8.0:2.0, 7.5:2.5, and 2.4:7.6 Pt:Ir immersion baths. In general, the unit cell dimensions of the NPs were in agreement with bulk solid solutions of Pt and Ir[59-64] and also support the assignment of the alloy structure as inferred from the STEM EDS data. The particle size does not change significantly with Pt:Ir mole ratio when the range of composition lies between ~60:40 and ~18:82.

In this study, the composition of the block copolymer templated Pt_xIr_{100-x} NPs was controlled by varying the ratio of $PtCl_6^{2-}$ to $IrCl_6^{2-}$ in the immersion baths. Characterization by XPS was used to determine the oxidation state and the relative content of Pt and Ir elements in the Pt_xIr_{100-x} NPs. The high-resolution XPS (HRXPS) plots for the 4f core electron regions were qualitatively similar for all Pt_xIr_{100-x} NPs synthesized from each of the two block copolymer templates. Fig. 3a depicts the HRXPS spectra for the Pt and Ir 4f core electron region for the NPs created from the PS_{1392}-*b*-$P4VP_{471}$ block copolymer template. From the peaks found in the bottom-most curve (curve i), monometallic Pt NPs exhibit two energy bands at 74.1 eV and 70.7 eV corresponding to Pt $4f_{5/2}$ and Pt $4f_{7/2}$ core electrons, respectively. The position of these peaks and the BE associated with the doublet splitting (ΔE = 3.4 eV), both strongly indicate the presence of metallic Pt(0).[65-67] From the peaks found in the top-most curve (curve viii), monometallic Ir NPs exhibit only two energy bands at 63.3 eV and 60.1 eV corresponding to Ir $4f_{5/2}$ and Ir $4f_{7/2}$ core electrons, respectively. Similarly, the position of these peaks, and the doublet splitting BE (ΔE = 3.2 eV), strongly indicate metallic Ir(0).[65-67]

The HRXPS plots of bimetallic Pt_xIr_{100-x} NPs are largely a combination of the spectra for the monometallic NPs, but with subtle differences that indicate mixing of the two metals. As the amount of Pt is decreased in favour of increased Ir content in the bimetallic NP analogues, the intensity of the Pt $4f_{5/2}$ and Pt $4f_{7/2}$ peaks decreases while that for Ir $4f_{5/2}$ and Ir $4f_{7/2}$ peaks increases. The BE of all peaks are largely indicative of a zero oxidation for Pt and Ir in the bimetallic NPs and exhibited little evidence for shoulders or secondary peaks at higher BE confirming the complete reduction of the $PtCl_6^{2-}$ and $IrCl_6^{2-}$ ions within the templates. As the Ir content is decreased in a template series, the Pt $4f_{5/2}$ and Pt $4f_{7/2}$ peaks were observed to shift to lower BE values, while those for the Ir $4f_{5/2}$ and Ir $4f_{7/2}$ had more constant BE values. The Pt $4f_{5/2}$ and Pt $4f_{7/2}$ BE

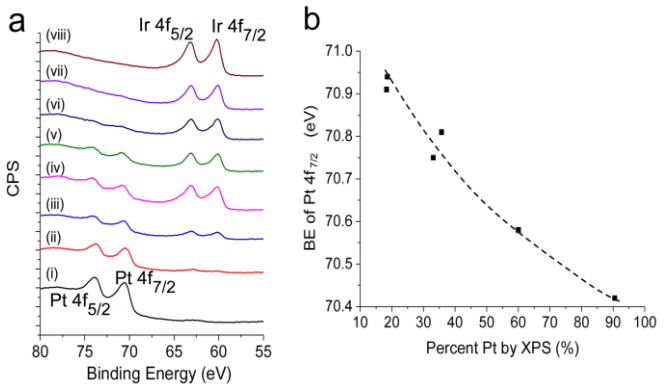

Fig. 3 (a) Offset HRXPS plots of PtIr NPs synthesized from PS_{1392}-*b*-$P4VP_{471}$ [the XPS-estimated composition of the PtIr NPs are (i) $Pt_{100}Ir_0$, (ii) $Pt_{91}Ir_9$, (iii) $Pt_{60}Ir_{40}$, (iv) $Pt_{33}Ir_{67}$, (v) $Pt_{36}Ir_{64}$, (vi) $Pt_{18}Ir_{82}$ [δ], (vii) $Pt_{19}Ir_{81}$, (viii) Pt_0Ir_{100}]. (b) Plot for the BE of the Pt $4f_{7/2}$ as a function of the atomic Pt percentage in the NPs as determined from the XPS analysis. The dotted line is intended to guide the eye.

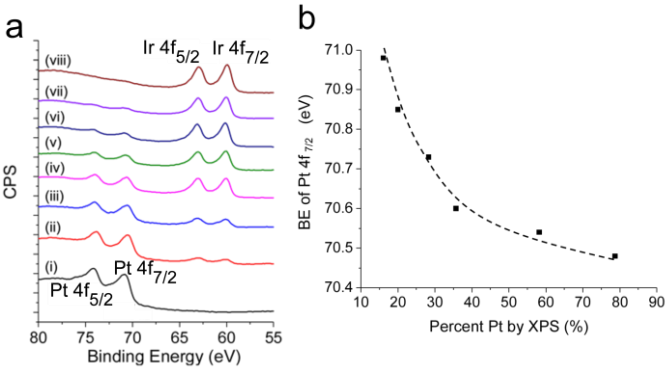

Fig. 4 (a) Offset HRXPS plots of PtIr NPs synthesized from PS_{552}-*b*-$P4VP_{174}$ [the XPS-estimated composition of the PtIr NPs are (i) $Pt_{100}Ir_0$, (ii) $Pt_{79}Ir_{21}$, (iii) $Pt_{58}Ir_{42}$, (iv) $Pt_{36}Ir_{64}$, (v) $Pt_{28}Ir_{72}$, (vi) $Pt_{20}Ir_{80}$, (vii) $Pt_{16}Ir_{84}$, (viii) Pt_0Ir_{100}]. (b) Plot for the BE of the Pt $4f_{7/2}$ as a function of the atomic Pt percentage in the NPs as determined from the XPS analysis. The dotted line is intended to guide the eye.

shift results from the electron transfer from Pt to Ir and is suggestive of highly mixed or alloyed Pt and Ir in the NPs.[68, 69] Shown in Fig. 3b is the plot of the BE for Pt $4f_{7/2}$ versus the XPS-determined percentage of Pt in the PtIr NPs in this series. A uniform trend in the BE for Pt $4f_{7/2}$ results as the amount of electronegative Ir is increased in the series.

The HRXPS characterization of the arrays of clusters of PtIr NPs created from the smaller length scale PS_{552}-*b*-$P4VP_{174}$ template was largely similar to that of the series of NPs from the higher molecular weight block copolymer template. The Pt $4f_{5/2}$ and Pt $4f_{7/2}$ peaks and Ir $4f_{5/2}$ and Ir $4f_{7/2}$ peaks of the monometallic Pt and Ir NPs indicated metallic characteristics and the intensity of each set of 4f peaks was tracked with the composition of Pt and Ir in the bimetallic analogues (see Fig. 4a). All 4f peaks exhibited little evidence for shoulders or secondary peaks at higher BE which confirms the complete reduction of the $PtCl_6^{2-}$ and $IrCl_6^{2-}$ anions in the templates as well. Similarly, as the Ir content is decreased in this series, the Pt $4f_{5/2}$ and Pt $4f_{7/2}$ peaks were observed to shift to lower BE values. Similar to data in Fig. 3b, the data in Fig. 4b show that the BE of the Pt $4f_{7/2}$ peak shifts to a lower BE as the XPS-determined percentage of Pt in the NPs increases; once again

confirming the charge transfer between the highly-mixed Pt and Ir, which supports an alloy phase for these particles. The extent of shifting of the Pt $4f_{7/2}$ peak is largely similar between the two polymer templates. The slope of the BE shift curves appear to differ slightly, which may be due to subtle effects caused by reduced NP size, charging effects from differing surface contamination or oxide formation unaccounted for in the analysis.[70]

The relative area of the Pt and Ir 4f peaks from the HRXPS plots is indicative of the composition of PtIr NPs. Curve fits were applied to each spectra in order to determine the intensity ratio and hence the atomic ratio of Pt:Ir in the NPs created from each template. Table 1 reports the NP composition in the format of Pt_xIr_{100-x} where the subscripts indicate the XPS-estimated atomic percentage of each metal. The PtIr ratios of Pt_xIr_{100-x} NPs created from the identical immersion baths, but with different templates are largely similar with only the NPs from the 9.5:0.5 and 2.4:7.6 immersion baths having a minor discrepancy. The composition data reported in Table 1 suggest that tailoring the composition of the immersion baths provides access to a wide compositional range for the PtIr bimetallic system regardless of the size-scale of the block copolymer template. The non-linear correlation between the Pt:Ir ratio of the immersion bath with the XPS-determined composition confirm that P4VP domains in the templates are preferentially loaded with $IrCl_6^{2-}$ ions during the immersion procedure (see Fig. S10). It should also be noted that the non-linear ion loading relationship resulted in identical XPS-determined composition for immersion baths 7.0:3.0 and 2.4:7.6 from the PS_{1392}-*b*-$P4VP_{471}$. The symbols δ and γ are used to distinguish between the two $Pt_{18}Ir_{82}$ compositions from the 7.0:3.0 and 2.4:7.6 baths, respectively (see Table S3).

Controlled Mass Loading of Pt and Ir into PtIr NP Arrays using Diblock Copolymer Templates

The block copolymer template approach for preparing PtIr NP arrays has several advantages that are reflected in mass loading profiles of the arrays relative to the bath composition. Platinum mass loading was determined by dissolving ITO-supported arrays of PtIr NPs in aqua regia and this data was combined with atomic ratio information to calculate the corresponding iridium mass loading values. Shown in Fig. 5a are the Pt and Ir mass loading values for a subset of the samples from Table 1. Trends in the mass loading values for the PtIr NPs arrays created from the two block copolymer templates are remarkably similar suggesting a highly-controlled NP fabrication procedure regardless of the selection of the template. Since the percentage of metals on the electrode surface is an important factor that influences the catalytic activity of catalysts, we have also used this data to determine the percentage of Pt and Ir on the electrode surface (see Fig. S11). For both series, as the platinum content in the loading baths is increased, a non-linear but tightly correlated increase in mass loading of Pt results in the NP arrays. The observed non-linear trend may be due to the instability of the Ir salts in the acidic aqueous media. Coordination of Ir with oxygen species from the aqueous media may lead to colloidal precipitates formed in solution.[71, 72] Shown in Fig. 5b are the total mass loading values for the same set of samples from Fig. 5a. The total mass loading values also appear to increase in a non-linear, but tightly correlated trend as the baths are enriched in $PtCl_6^{2-}$ rather than $IrCl_6^{2-}$. The higher and lower molecular weight block copolymer templates create PtIr NPs with an overall metal loading in the ranges of ~0.2 to 0.7 μg/cm^2 and 0.2 to 1 μg/cm^2,

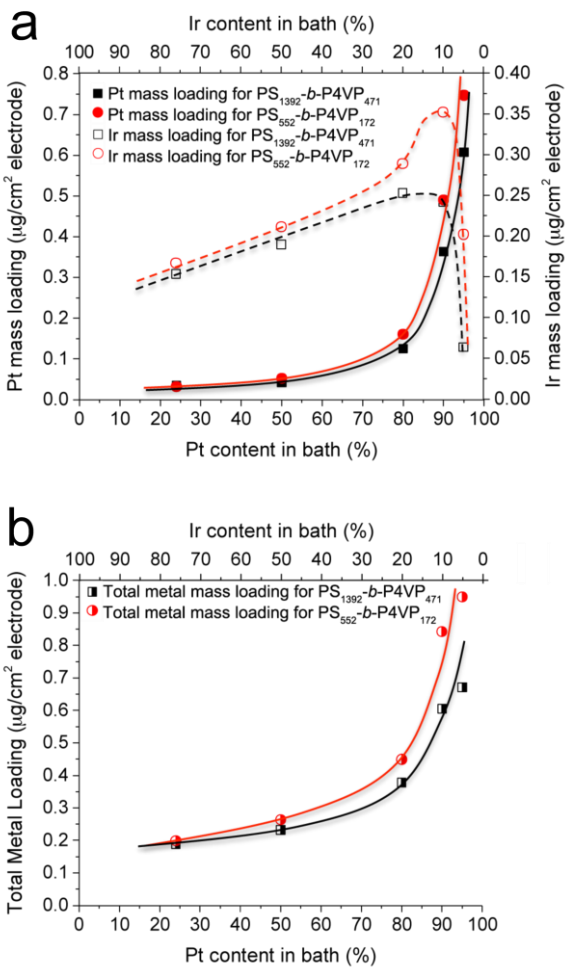

Fig. 5 (a) Mass loading data for Pt and Ir quantified by ICP-MS and plotted against % Pt and Ir content present in the loading baths for NPs synthesized from PS_{1392}-*b*-$P4VP_{471}$ and PS_{552}-*b*-$P4VP_{174}$. (b) Total mass loading by polymer template.

respectively. Achieving highly mixed metals in well-defined NPs confirm that the synthetic approach involving block copolymer thin film templates is a simple but powerful method to access distinct compositions of bimetallic NP arrays. Other experimental factors that define the metal loading procedure, including total metal anion concentration, anion valency, pH, ionic strength, immersion time, and temperature are expected to tune the mass loading profiles shown in Fig. 5a-b. The highly correlated mass-loading profiles that result from this NP fabrication approach are advantageous in understanding variations in catalytic performance (*vide infra* for formic acid oxidation analysis).

Electrochemical Surface Area (ECSA) of PtIr NP Arrays – CO Stripping Voltammetry

The ECSA values of selected PtIr catalysts from each polymer series were determined. The carbon monoxide stripping approach for the

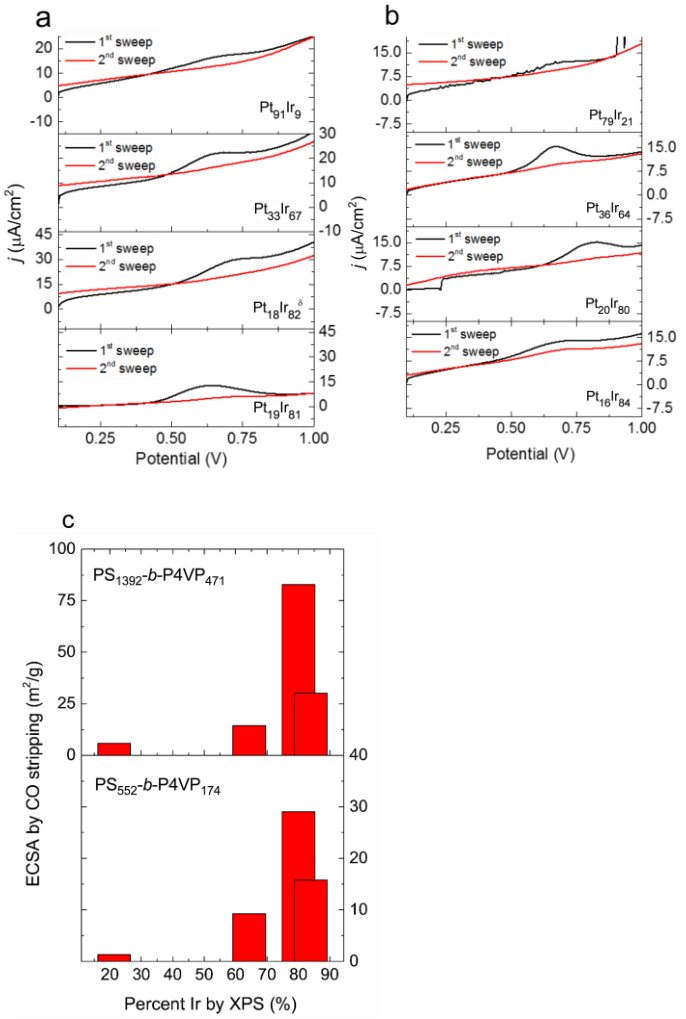

Fig. 6 (a-b) Anodic current density (*j*) vs. potential of CO oxidative stripping CV plots for selected Pt_xIr_{100-x} NPs synthesized from the two block copolymer templates. The potential is referenced against Ag/AgCl. Data from the first anodic sweep (with a CO oxidation peak) is shown in black while data from the second anodic sweep is shown red. The inset Pt_xIr_{100-x} labels report the XPS-estimated composition of the NPs formed from (a) PS_{1392}-*b*-$P4VP_{471}$ and (b) PS_{552}-*b*-$P4VP_{174}$. (c) Bar chart summary of ECSA values for catalysts studied in (a) and (b).

determination of ECSA from voltammetry relies on forming a monolayer of strongly adsorbed carbon monoxide (CO) molecules onto the surfaces of the nanocatalysts. A linear, atop binding of CO onto metal surface atoms is assumed and that the coulombic charge required to subsequently oxidize this type of CO layer to CO_2 is equal to 420 μC/cm^2 of catalyst.[73, 74] In this work, the CO oxidative stripping CV experiments are conducted with Ar-sparged electrolyte and a constant headspace of Ar immediately after a potentiostatic CO adsorption step (E = 0.10 V; 5 min).[37] Shown in Fig. 6 are the plots for two sequential anodic sweeps for the CO-stripping CV experiment for selected Pt_xIr_{100-x} NPs. In both anodic traces, the capacitive charging of the electrochemical cell is responsible for the current associated with the baseline. In the first anodic sweep of all PtIr catalysts, an oxidation peak develops with peak current values for CO oxidation in the range of 0.63 to 0.68 V. The current profiles and peak potentials are largely in agreement with those previously reported for NPs studied under similar conditions.[75] The area of this peak relative to the capacitive charging baseline in the second anodic sweep represents the total charge associated with CO oxidation. The ECSA (in cm^2 catalyst/g) is calculated according to Eq. (1):

$$ECSA = \frac{Q_{CO}}{M_l \times (420\ \frac{\mu C}{cm^2})} \quad (1)$$

where Q_{co}, is the measured charge associated with CO oxidation in μC/cm^2 electrode, and M_l represents the total metal mass loading in μg/cm^2 electrode. The ECSA values for each catalyst in the two polymer series are reported in Fig. 6c. The ECSA values of the PtIr values would be higher for the NP arrays with a higher population of NPs and larger geometric surface areas (a result of the higher diameter values). Within each polymer series, there appears to be a maximum ECSA where NPs consisting of ~80% Ir (by XPS) exhibit ECSA values of 84 m^2 catalyst/g and 29 m^2 catalyst/g for the PtIr catalysts produced from PS_{1392}-*b*-$P4VP_{471}$ and PS_{552}-*b*-$P4VP_{174}$ templates, respectively.

Electrocatalytic Oxidation of Formic Acid by PtIr Bimetallic NP Arrays

The electrocatalytic activity of NP catalysts for the HCOOH oxidation reaction is typically studied using CV at low pH.[18, 76, 77] In this work, we focus on the electrochemical activity of the bimetallic catalysts for the oxidation of formic acid. The catalytic performance of the monometallic Pt and Ir catalysts produced from the two block copolymers is provided in the Supporting Information (Fig. S12). For reference, a labelled HCOOH oxidation CV curve is shown in

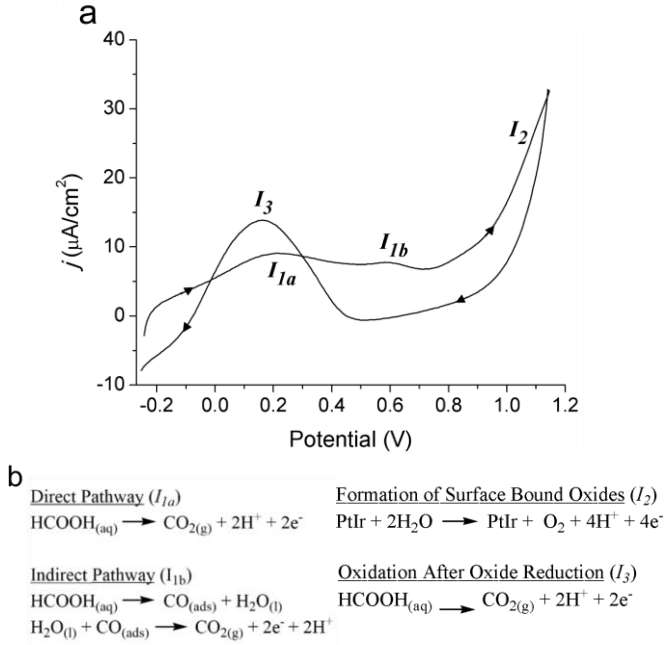

Fig. 7 (a) Representative HCOOH oxidation CV (11th cycle from $Pt_{79}Ir_{21}$ NP from PS_{552}-*b*-$P4VP_{174}$) for one complete cycle outlining peaks of interest. (b) Relevant electrochemical steps (I_{1a}, I_{1b}, I_2 and I_3).

Fig. 7a with relevant electrochemical steps for this potential range outlined in Fig. 7b. The anodic sweep typically exhibits three positive peaks while the cathodic sweep exhibits a single positive peak. The first anodic peak (I_{1a}) occurs at ~ 0.2 V and corresponds to the direct oxidation of HCOOH to CO_2 by the dehydrogenation reaction, listed at the top of Fig. 7b. A second anodic peak (I_{1b}) at ~ 0.6 V, indicates the indirect oxidation pathway for formic acid through an adsorbed CO intermediate.[18, 76, 77] Adsorbed CO (CO_{ads}) intermediates formed in the dehydrogenation pathway occur after the formation of surface hydroxides at 0.5 V.[78] Ir-rich NPs are particularly advantageous for these steps due to the
favourable binding of oxygen-rich species to Ir sites at low potentials and, thus, favouring complete oxidation of adsorbed intermediates including CO_{ads}. Consequently, the reaction mechanism for PtIr is bifunctional.[79, 80] As potential continues beyond 0.7 V the HCOOH oxidation ceases and the oxygen evolution reaction occurs at the surfaces of the catalyst, represented by current peak I_2.[81] During the reverse cathodic sweep, small amounts of HCOOH act as a local reducing agent for the surface oxides. Reduction of the catalyst surfaces allow for reinitiation of catalytic oxidation of HCOOH (I_3 peak).

In order to assess the catalytic activity of block copolymer-derived arrays of bimetallic Pt_xIr_{100-x} NP arrays for the formic acid oxidation reaction, a 25-cycle CV experiment was conducted (Fig. S8a and S8b in the Supporting Information). The current information was combined with the mass loading information in order to report CV curves in a specific current format (in units of A/g catalyst). The representative CV plots acquired after stabilization (15th cycle) for HCOOH oxidation for the Pt_xIr_{100-x} NPs synthesized from the two block copolymers are reported in Fig. 8a and 8b. The Fig. 8c and 8d report the evolution of the maximum current density for I_{1a} with cycle number for each series of Pt_xIr_{100-x} NP clusters and the analogous plots for I_3 are found in the Supporting Information file (Fig. S13 and S14). Precisely estimating peak current values for I_{1b}, and I_2 during each cycle was not possible for all cycles for each catalyst and are not included in this study. In general, the I_{1a} mass-specific peak current values were higher for bimetallic catalysts afforded from the smaller block copolymer. The most active NP catalyst clusters created from the PS_{1392}-*b*-$P4VP_{471}$ and PS_{552}-*b*-$P4VP_{174}$ templates for the I_{1a} pathway during the 25 cycles were $Pt_{18}Ir_{82}{}^{\gamma}$ (cycle 5; 24 A/g) and $Pt_{16}Ir_{84}$ (cycle 3; 37 A/g), respectively. It is logical that Ir-rich catalysts would be more active during these steps due to the favourable binding of oxygen containing species by Ir.

The increasing binding energy for Pt (Fig. 3b and 4b) suggests that the bond strength of adsorbed key intermediates for formic acid oxidation may also be affected by the Pt:Ir ratio. Fig. S16 in the supporting information file reports possible correlations between the catalyst activity for the I_{1a} pathway with the BE of the $Pt4f_{7/2}$ peak found by XPS. Using the peak current for I1a as a metric for catalyst activity, it was found that the cycle 3 activity of Pt_xIr_{100-x} NPs produced from the PS_{1392}-*b*-$P4VP_{471}$ roughly followed a volcano-type trend with the BE of Pt $4f_{7/2}$. By cycle 15, this correlation was lost, perhaps indicating a change in the surface composition and/or structure of the catalysts away from the condition of samples studied in the XPS section above. Other factors such as interparticle and intercluster spacing are expected to contribute to this catalytic activity as well. A more consistent correlation in the dependency of the cycle 3 and cycle 15 catalytic activity on BE of Pt $4f_{7/2}$ was found for Pt_xIr_{100-x} NPs synthesized using the smaller PS_{552}-b-$P4VP_{174}$, which suggests a more consistent NP structure and condition over many cycles of catalysis. An interesting plateau in the dependency of the I_{1a} catalyst activity was found for this series, suggesting that the surface bonding characteristics that are associated with Pt binding energy are not the ultimate factor for determining the catalyst activity. The elucidation of which factors affect activity and stability and their evolution with ongoing catalyst cycle number is past the scope of this study and represents a topic of current research. After stabilization, the I_{1a} mass activity values were found to be close to that of other work.[82-84] Interestingly, the most active NP catalyst clusters created from the PS_{1392}-*b*-$P4VP_{471}$ and PS_{552}-*b*-$P4VP_{174}$ templates for the I_3 pathway during the 25 cycles were $Pt_{91}Ir_9$ (cycle 5; 32 A/g) and $Pt_{79}Ir_{21}$ (cycle 3; 19 A/g), respectively. The shift in catalyst activity to a more Pt-rich NP catalyst for the I_3

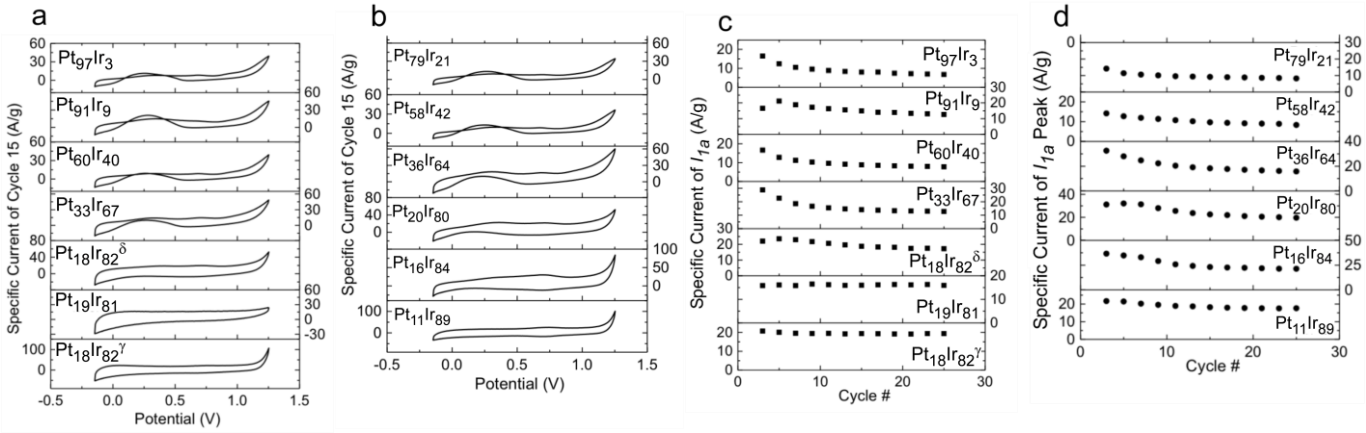

Fig. 8 Representative CV plots acquired after stabilization. The 15th CV cycle of selected bimetallic catalysts of PtIr NP arrays synthesized from (a) PS_{1392}-*b*-$P4VP_{471}$ and (b) PS_{552}-*b*-$P4VP_{174}$. (c) Specific current (normalized for mass loading) for I_{1a} versus cycle number for the same catalysts studied in (a). (d) Specific current (normalized for mass loading) for I_{1a} versus cycle number for the same catalysts studied in (b). All PtIr NP arrays are supported on ITO. The CV data was acquired in 100 mM HCOOH and 100 mM H_2SO_4. The subscripts in the label denote the XPS-estimated composition.

pathway is due to surface contamination (i.e. poisoning) that results from incomplete formic acid oxidation reactions that occur prior to I_2 current and limit I_{1a} and I_{1b} processes. The highly oxidizing conditions that arise during the I_2 pathway decontaminate the surfaces of these catalysts and may permit otherwise poisoned surfaces to contribute to the current in the I_3 peak. Since Pt is known to poison easily, it is reasonable that more Pt-rich bimetallic catalysts will show improved activity immediately following a high potential oxidation like that established during the generation of the current for I_2. Alloyed PtRu is an industry and research standard for fuel cell anode development.[85] A commercial (BASF) carbon-supported PtRu catalyst was recently investigated for HCOOH electrooxidation under similar conditions. Mass activities of 11 and 30 A/g were reported for I_{1a} and I_3, respectively.[86] Many of the bimetallic PtIr NPs isolated from the block copolymer template approach are higher in activity than this industry/research standard as well as others (see Table S1 in the Supporting Information file). The multi-cycle activity of these bimetallic catalysts was evaluated using $Pt_{18}Ir_{82}$[δ] and $Pt_{20}Ir_{80}$ from immersion bath 7.0:3.0 as representative arrays of NPs for the series.

In general, the PtIr NPs show significant formic acid activity for more than 200 cycles of oxidation (see Supporting Information file, Fig. S17). A four-fold increase in mass activity was demonstrated for the $Pt_{16}Ir_{84}$ catalyst from the PS_{552}-*b*-$P4VP_{174}$ template when compared to the I_{1a} pathway for a BASF commercial standard. The block copolymer template approach is, therefore, a highly relevant method for creating highly active and durable electrocatalysts for the formic acid oxidation reaction. Previous research has suggested that a 2-nm diameter $Pt_{50}Ir_{50}$ NP exhibits a maximum current density for compositionally varied PtIr catalysts for the I_{1a} pathway for formic acid oxidation.[76] Previous work has shown that the minimum feature size of block copolymers can be less than 5 nm.[87-90] The block copolymer template approach described herein has shown that bimetallic catalysts often have diameters are smaller than the micelle feature size in the template. We, therefore, expect that very low

The ECSA values from Fig. 6 were combined with selected CV data and used to report the ECSA-specific current in Fig. 9. It is still apparent that the catalytic activity of the arrays of PtIr NPs afforded from the smaller block copolymer template are more active than those created from the larger block copolymer derivative. Since the identification of a near-optimal composition for PtIr catalyst for HCOOH oxidation has already been reported,[77] we direct our attention to general comparisons between NP catalysts between polymer analogues. It is reasonable to conclude that the mass loading or the ECSA parameters are not the only properties that lead to the differences in catalytic activity within a polymer series. Recent work has shown that the activation of water at both the catalyst surface as well as at the surface of oxide support materials (ITO in this case) can increase the population of surface hydroxyl groups, which is a major factor in the removal of rate-limiting carbonaceous intermediates and may play a role in the mechanism for the catalytic oxidation of formic acid and any adsorbed CO (CO_{ads}).[91] The ITO electrode support used in this work is comprised of a complex polycrystalline bixbyite-type indium tin oxide whose surface hydroxyl distribution is complex and sensitive to surface treatments.[92] Indeed the exact surface composition of ITO films is often debated.[93, 94] The population of surface hydroxyl groups on

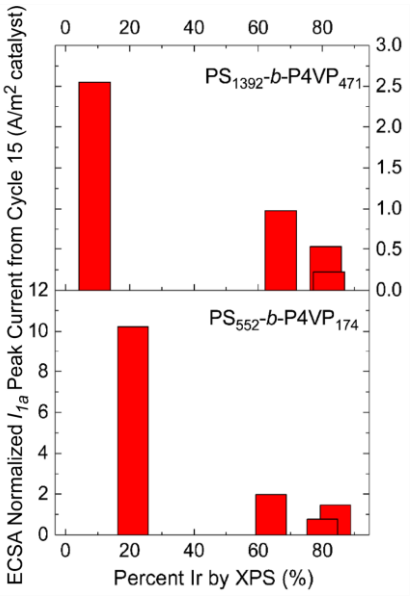

Fig. 9 Plots of the ECSA-specific current for the I_{1a} peak in cycle 15 for selected Pt_xIr_{100-x} catalysts prepared from PS_{1392}-*b*-$P4VP_{471}$ (top) and PS_{552}-*b*-$P4VP_{174}$ (bottom).

diameter bimetallic NPs can be accessed from lower molecular weight templates with smaller micellar feature size and may permit more fundamental studies, such as stability, coarsening, cluster definition, uniform mass loading, and the effect of catalyst distribution.

The identification of high activity bimetallic catalysts for the HCOOH oxidation reaction (on a mass loading basis) warrants an analysis of the ECSA. It is clear from Fig. 8c and 8d that the electrocatalytic activity of the Pt_xIr_{100-x} NPs evolve to lower values with cycle number, but stabilize to a non-zero value at ~ 15 cycles. The discussion of the ECSA-specific current, therefore, focuses on catalyst activity associated with CV traces in the 15th cycle. both the surface of the bimetallic NP catalysts and the substrate need to be carefully understood and better quantified in order to understand the catalytic activity of ITO-supported arrays of PtIr NP catalysts for the formic oxidation reaction.

Conclusions

Controlled syntheses of Pt-based electrochemical catalysts that specify the structure and stoichiometry on the nanoscale are of great importance to energy technologies. Arrays of PtIr alloy NP clusters are synthesized from an approach using block copolymer templates. The block copolymer template method allowed for both relatively narrow diameter distributions (~4 – 13 nm) and uniform intercluster spacing (~60 or ~100 nm) to be established in this work. The reconstruction of spin coated PS-*b*-P4VP block copolymer micelle films into an array of pyridinium-rich domains defines a template that is capable of electrostatically loading $PtCl_6^{2-}$ and $IrCl_6^{2-}$ anions into a periodic array. Both anionic species are simultaneously loaded into the template from low-pH aqueous immersion baths with codissolved hexachloroplatinic and hexachloroiridic acid. The thermoreductive annealing under inert atmosphere at 600°C simultaneously reduces the metal anions, alloys the resulting metals,

and degrades the block copolymer template. The HRTEM studies confirm that each pyridinium-rich domain yields NPs and in some cases clusters of crystalline PtIr NP alloys with the number of NPs determined by the size of the pyridinium-rich domain of the block copolymer template. The composition of the NPs was determined by EDS and XPS and is set by the ratio of anions in the loading bath. A non-linear relationship between the Pt:Ir ratio in the loading baths with the Pt:Ir ratio in the NPs was found. The NP lattice characterization by STEM-EDS, the BE shift of Pt 4f core electrons and the shift in the potential for the oxide reduction as observed from the CV measurements further support the formation of an alloy structure in the NPs. Catalytic activity for the formic acid oxidation reaction was studied by CV and shows that the arrays of clusters of PtIr alloy NPs are highly active catalysts with mass activity values of 24 A/g and 37 A/g for the $Pt_{18}Ir_{82}$ and $Pt_{16}Ir_{84}$ from the PS_{1392}-*b*-$P4VP_{471}$ and PS_{552}-*b*-$P4VP_{174}$, respectively. Many of the bimetallic PtIr NPs isolated from the block copolymer template approach are much higher in activity than typical industry/research standards. The most active array of $Pt_{16}Ir_{84}$ NPs had mass activities for HCOOH oxidation that were four-fold higher than that of a PtRu industrial research standard. The arrayed NP catalysts like those described herein continue to offer advantages owing to their ease of fabrication and their well-defined size, shape, spacing and allow for model studies that lead to more insight into the mechanistic aspects of electrocatalysis.[95-96] Generally, we expect that this approach for creating bimetallic catalysts from block copolymer templates will be more applicable in the future as more active and more inexpensive metals are investigated. Therefore, a block copolymer template-based method of preparing highly active clusters of low-diameter, PtIr NPs will have a positive impact on several emerging areas in nanoscience, such as energy devices, solar fuels, and heterogeneous catalysis.

Acknowledgements

This work was supported in part by a faculty start-up grant from the Advanced Materials Science and Engineering Center at Western Washington University (AMSEC WWU) and by external grants from the American Chemical Society Petroleum Research Fund (ACS-PRF UNI # 51559-UNI10 and ACS-PRF UR # 54780-UR10) and Research Corporation (# 21109). Further support was provided in part by the Natural Sciences and Engineering Research Council (NSERC) of Canada (Grant # 1077758) and the Canada Research Chairs Program (B.D. Gates, Grant # 950-215846). This work made use of 4D LABS (www.4dlabs.ca) shared facilities (Simon Fraser University) supported by the Canada Foundation for Innovation (CFI), British Columbia Knowledge Development Fund (BCKDF), Western Economic Diversification Canada, and Simon Fraser University. A portion of the research was performed using EMSL, a DOE Office of Science User Facility sponsored by the Office of Biological and Environmental Research and located at Pacific Northwest National Laboratory (User Facility Grant # 48182). The authors are thankful to Libor Kovarik for assistance with TEM data. AT is grateful for a graduate research grant from the Vice Provost for Research at WWU and to Benjamin Morgan for helpful discussions.

References

1. S. Ha; B. Adams; R. Masel, *J. Power Sources* 2004**, *128*** (2), 119-124.
2. X. Yu; P. G. Pickup, *J. Power Sources* 2008**, *182*** (1), 124-132.
3. Y. Zhu; S. Y. Ha; R. I. Masel, *J. Power Sources* 2004**, *130*** (1), 8-14.
4. O. T. Holton; J. W. Stevenson, *Platinum Met. Rev.* 2013**, *57*** (4), 259-271.
5. J. Zhang, *PEM fuel cell electrocatalysts and catalyst layers: fundamentals and applications*. Springer Science & Business Media: 2008; p 165-287.
6. S. Wasmus; A. Küver, *J. Electroanal. Chem.* 1999**, *461*** (1), 14-31.
7. K. Yasuda; S. Miyata, Durability Targets for Stationary and Automotive Applications in Japan. In *Polymer Electrolyte Fuel Cell Durability*, Springer: 2009; p 489-496.
8. R. Wang; C. Wang; W. B. Cai; Y. Ding, *Adv. Mater.* 2010**, *22*** (16), 1845-1848.
9. E. Uggerud; C. Adlhart, *Chem. Commun.* 2006**,** (1), 2581-2582.
10. Y. Sun; L. Zhuang; J. Lu; X. Hong; P. Liu, *J. Am. Chem. Soc.* 2007**, *129*** (50), 15465-15467.
11. K. Yamamoto; T. Imaoka; W.-J. Chun; O. Enoki; H. Katoh; M. Takenaga; A. Sonoi, *Nat. Chem.* 2009**, *1*** (5), 397-402.
12. F. Hasché; M. Oezaslan; P. Strasser, *J. Electrochem. Soc.* 2011**, *159*** (1), B24-B33.
13. N. S. Sobal; U. Ebels; H. Möhwald; M. Giersig, *J. Phys. Chem. B* 2003**, *107*** (30), 7351-7354.
14. C. Rice; S. Ha; R. Masel; A. Wieckowski, *J. Power Sources* 2003**, *115*** (2), 229-235.
15. J. Zhang; F. Lima; M. Shao; K. Sasaki; J. Wang; J. Hanson; R. Adzic, *J. Phys. Chem. B* 2005**, *109*** (48), 22701-22704.
16. P. Strasser; M. Oezaslan; F. Hasché; S. Koh; C. Yu; R. Srivastava, *Chem. Ing. Tech.* 2008**, *80*** (9), 1267.
17. M. Zeng; X. X. Wang; Z. H. Tan; X. X. Huang; J. N. Wang, *J. Power Sources* 2014**, *264***, 272-281.
18. Q. Yi; A. Chen; W. Huang; J. Zhang; X. Liu; G. Xu; Z. Zhou, *Electrochem. Commun.* 2007**, *9*** (7), 1513-1518.
19. A. Allagui; M. Oudah; X. Tuaev; S. Ntais; F. Almomani; E. A. Baranova, *Int. J. Hydrogen Energy* 2013**, *38*** (5), 2455-2463.
20. E. Gyenge; M. Atwan; D. Northwood, *J. Electrochem. Soc.* 2006**, *153*** (1), A150-A158.
21. M. B. Vukmirovic; J. Zhang; K. Sasaki; A. U. Nilekar; F. Uribe; M. Mavrikakis; R. R. Adzic, *Electrochim. Acta* 2007**, *52*** (6), 2257-2263.
22. K.-J. Chen; K. C. Pillai; J. Rick; C.-J. Pan; S.-H. Wang; C.-C. Liu; B.-J. Hwang, *Biosens. Bioelectron.* 2012**, *33*** (1), 120-127.
23. Y. M. López-De Jesús; A. Vicente; G. Lafaye; P. Marécot; C. T. Williams, *J. Phys. Chem. C* 2008**, *112*** (36), 13837-13845.
24. T. Miyao; K. Minoshima; S. Naito, *J. Mater. Chem.* 2005**, *15*** (23), 2268-2270.
25. J. R. Croy; S. Mostafa; L. Hickman; H. Heinrich; B. R. Cuenya, *Applied Catalysis A: General* 2008**, *350*** (2), 207-216.
26. L. K. Ono; B. Roldán-Cuenya, *Catal. Lett.* 2007**, *113*** (3-4), 86-94.

27. D. A. Boyd; Y. Hao; C. Li; D. G. Goodwin; S. M. Haile, *ACS nano* 2013**, *7*** (6), 4919-4923.
28. K. Mikkelsen; B. Cassidy; N. Hofstetter; L. Bergquist; A. Taylor; D. A. Rider, *Chem. Mater.* 2014**, *26*** (24), 6928-6940.
29. E. Ehret; E. Beyou; G. Mamontov; T. Bugrova; S. Prakash; M. Aouine; B. Domenichini; F. C. S. Aires, *Nanoscale* 2015**, *7*** (31), 13239-13248.
30. J. P. Spatz; S. Mössmer; C. Hartmann; M. Möller; T. Herzog; M. Krieger; H.-G. Boyen; P. Ziemann; B. Kabius, *Langmuir* 2000**, *16*** (2), 407-415.
31. J. Shim; J. Lee; Y. Ye; J. Hwang; S.-K. Kim; T.-H. Lim; U. Wiesner; J. Lee, *ACS nano* 2012**, *6*** (8), 6870-6881.
32. S. C. Warren; M. R. Perkins; A. M. Adams; M. Kamperman; A. A. Burns; H. Arora; E. Herz; T. Suteewong; H. Sai; Z. Li, *Nat. Mater.* 2012**, *11*** (5), 460-467.
33. J. H. Mun; Y. H. Chang; D. O. Shin; J. M. Yoon; D. S. Choi; K.-M. Lee; J. Y. Kim; S. K. Cha; J. Y. Lee; J.-R. Jeong, *Nano Lett.* 2013**, *13*** (11), 5720-5726.
34. M. Aizawa; J. M. Buriak, *J. Am. Chem. Soc.* 2006**, *128*** (17), 5877-5886.
35. J. Chai; J. M. Buriak, *ACS nano* 2008**, *2*** (3), 489-501.
36. B. R. Chalamala; Y. Wei; R. H. Reuss; S. Aggarwal; S. R. Perusse, *J. Vac. Sci. & Technol.* 2000**, *18*** (4), 1919-1922.
37. P. Urchaga; S. v. Baranton; C. Coutanceau; G. Jerkiewicz, *Langmuir* 2011**, *28*** (7), 3658-3663.
38. S. Park; J.-Y. Wang; B. Kim; W. Chen; T. P. Russell, *Macromolecules* 2007**, *40*** (25), 9059-9063.
39. B.-H. Sohn; S.-I. Yoo; B.-W. Seo; S.-H. Yun; S.-M. Park, *J. Am. Chem. Soc.* 2001**, *123*** (50), 12734-12735.
40. G. Riess, *Prog. Polym. Sci.* 2003**, *28*** (7), 1107-1170.
41. F. Calderara; G. Riess, *Macromol. Chem. Phys.* 1996**, *197*** (7), 2115-2132.
42. J. Bansmann; S. Kielbassa; H. Hoster; F. Weigl; H.-G. Boyen; U. Wiedwald; P. Ziemann; R. Behm, *Langmuir* 2007**, *23*** (20), 10150-10155.
43. L. Wang; F. Montagne; P. Hoffmann; R. Pugin, *Chem. Commun.* 2009**,** (25), 3798-3800.
44. S. Yoo; H. Cho; J. P. Lee; K. T. Kim; S. Park, *Chemistry–An Asian Journal* 2012**, *7*** (4), 692-695.
45. H. Cho; S. Choi; J. Y. Kim; S. Park, *Nanoscale* 2011**, *3*** (12), 5007-5012.
46. X. Zu; X. Hu; L. A. Lyon; Y. Deng, *Chem. Commun.* 2010**, *46*** (42), 7927-7929.
47. A. Fernandez-Nieves; A. Fernandez-Barbero; B. Vincent; F. De las Nieves, *Macromolecules* 2000**, *33*** (6), 2114-2118.
48. A. Loxley; B. Vincent, *Colloid. Polym. Sci.* 1997**, *275*** (12), 1108-1114.
49. N. Tantavichet; M. D. Pritzker; C. M. Burns, *J. Appl. Polym. Sci.* 2001**, *81*** (6), 1493-1497.
50. C. Ripoll; G. Muller; E. Selegny, *Eur. Polym. J.* 1971**, *7*** (10), 1393-1409.
51. L. M. Bronstein; S. N. Sidorov; P. M. Valetsky; J. Hartmann; H. Cölfen; M. Antonietti, *Langmuir* 1999**, *15*** (19), 6256-6262.
52. F. Behafarid, B. R. Cuenya, *Surf. Sci.* **2012**, 606 (11), 908-918.
53. F. Behafarid, B. Roldan Cuenya, *Top. Catal.* **2013**, 56 (15), 1542–1559.
54. J. Matos, L.K. Ono, F. Behafarid, J.R. Croy, S. Mostafa, A. T. DeLaRiva, A.K. Datye, A.I. Frenkel, B. Roldan Cuenya, *Phys. Chem. Chem. Phys.* **2012**, 14 (32), 11457-11467.
55. A. Aramata; T. Yamazaki; K. Kunimatsu; M. Enyo, *J. Phys. Chem.* 1987**, *91*** (9), 2309-2314.
56. S. Wang; U. Kürpick; G. Ehrlich, *Phys. Rev. Lett.* 1998**, *81*** (22), 4923-4926.
57. C. Alonso; R. Salvarezza; J. Vara; A. Arvia; L. Vazquez; A. Bartolome; A. Baro, *J. Electrochem. Soc.* 1990**, *137*** (7), 2161-2166.
58. A. A. Gambardella; N. S. Bjorge; V. K. Alspaugh; R. W. Murray, *J. Phys. Chem. C* 2011**, *115*** (44), 21659-21665.
59. J. Xu; T. Zhao; W. Yang; S. Shen, *Int. J. Hydrogen Energy* 2010**, *35*** (16), 8699-8706.
60. J. Chen; T. Herricks; M. Geissler; Y. Xia, *J. Am. Chem. Soc.* 2004**, *126*** (35), 10854-10855.
61. E. Irissou; F. Laplante; S. Garbarino; M. Chaker; D. Guay, *J. Phys. Chem. C* 2010**, *114*** (5), 2192-2199.
62. H. Okamoto; T. Massalski, *Bulletin of Alloy Phase Diagrams* 1985**, *6*** (1), 46-56.
63. A. Suzuki; M. Harada; Y. Wu; H. Murakami, *Mater. Trans.* 2005**, *46*** (8), 1760-1763.
64. R. Bedford; G. Bonnier; H. Maas; F. Pavese, *Metrologia* 1996**, *33*** (2), 133-154.
65. J. Shyu; K. Otto, *Appl. Surf. Sci.* 1988**, *32*** (1), 246-252.
66. M. Engelhard; D. Baer, *Surf. Sci. Spectra* 2000**, *7*** (1), 1-68.
67. R. Nyholm; A. Berndtsson; N. Martensson, *J. Phys. C: Solid State* 1980**, *13*** (36), L1091-L1096.
68. X. Ge; X. Yan; R. Wang; F. Tian; Y. Ding, *J. Phys. Chem. C* 2009**, *113*** (17), 7379-7384.
69. Z. Bastl; Š. Pick, *Surf. Sci.* 2004**, *566***, 832-836.
70. J. Zhang; D. N. Oko; S. b. Garbarino; R. g. Imbeault; M. Chaker; A. C. Tavares; D. Guay; D. Ma, *J. Phys. Chem. C* 2012**, *116*** (24), 13413-13420.
71. J. M. Sanchez; V. Salvado; J. Havel, *J. Chromotag. A* 1999, **834**(1), 329-340.
72. S. E. Livingston; J. C. Bailar; H. J. Emeleus; R. Nyholm; A. F. Trotman, *Comprehensive Inorganic Chemistry, Vol. 3*, Pergamon: 1975; p 1254-1274.
73. Z. B. Wang; P. J. Zuo; G. P. Yin, *Fuel Cells* 2009**, *9*** (2), 106-113.
74. E. I. Santiago; G. A. Camara; E. A. Ticianelli, *Electrochim. Acta* 2003**, *48*** (23), 3527-3534.
75. J. Solla-Gullón; F. Vidal-Iglesias; E. Herrero; J. Feliu; A. Aldaz, *Electrochem. Commun.* 2006**, *8*** (1), 189-194.
76. A. Capon; R. Parsons, *J Electroanal Chem Interfacial Electrochem* 1973**, *44*** (2), 239-254.
77. W. Chen; S. Chen, *J. Mater. Chem.* 2011**, *21*** (25), 9169-9178.
78. G. A.Nagar; A. M. Mohammad; M. S. El-Deab; B. E. El-Anadouli, *ACS Appl. Mater. Inter.* 2012, **606** (11), 908-918.
79. L. Ouattara; S. Fierro; O. Frey; M. Koudelka; C. Comninellis, *J. Appl. Electrochem.* 2009**, *39*** (8), 1361-1367.
80. J.-H. Choi; K.-J. Jeong; Y. Dong; J. Han; T.-H. Lim; J.-S. Lee; Y.-E. Sung, *J. Power Sources* 2006**, *163*** (1), 71-75.
81. N. Danilovic; R. Subbaraman; K. Chang; S. H. Chang; Y. J. Kang ; J. Snyder ; A. P. Paulikas D. Strmcnik; Y. Kim; D. Myers; V. R. Stamenkovic; N. M. Markovic, *J. Phys. Chem. Lett.* 2014, **5** (14), 2474-2478.

82. J. Jiang; A. Kucernak, *J. Electroanal. Chem.* 2002**, *520*** (1), 64-70.
83. C.-H. Jung; T. Zhang; B.-J. Kim; J.-D. Kim; C.-K. Rhee; T.-H. Lim, *Bull. Korean Chem. Soc.* 2010**, *31*** (6), 1543-1550.
84. E. Spinacé; R. R. Dias; M. Brandalise; M. Linardi; A. O. Neto, *Ionics* 2010**, *16*** (1), 91-95.
85. C. Roychowdhury; F. Matsumoto; V. B. Zeldovich; S. C. Warren; P. F. Mutolo; M. Ballesteros; U. Wiesner; H. D. Abruña; F. J. DiSalvo, *Chem. Mater.* 2006**, *18*** (14), 3365-3372.
86. Y. Lu; W. Chen, *Chem. Commun.* 2011**, *47*** (9), 2541-2543.
87. S. Park; D. H. Lee; J. Xu; B. Kim; S. W. Hong; U. Jeong; T. Xu; T. P. Russell, *Science* 2009**, *323*** (5917), 1030-1033.
88. J. D. Cushen; C. M. Bates; E. L. Rausch; L. M. Dean; S. X. Zhou; C. G. Willson; C. J. Ellison, *Macromolecules* 2012**, *45*** (21), 8722-8728.
89. J. D. Cushen; I. Otsuka; C. M. Bates; S. Halila; S. Fort; C. Rochas; J. A. Easley; E. L. Rausch; A. Thio; R. Borsali, *ACS nano* 2012**, *6*** (4), 3424-3433.
90. J. G. Kennemur; L. Yao; F. S. Bates; M. A. Hillmyer, *Macromolecules* 2014**, *47*** (4), 1411-1418.
91. C. Bock; B. MacDougall, *Electrochim. Acta* 2002**, *47*** (20), 3361-3373.
92. C. Donley; D. Dunphy; D. Paine; C. Carter; K. Nebesny; P. Lee; D. Alloway; N. R. Armstrong, *Langmuir* 2002**, *18*** (2), 450-457.
93. T. Ishida; H. Kobayashi; Y. Nakato, *J. Appl. Phys.* 1993**, *73*** (9), 4344-4350.
94. A. Nelson; H. Aharoni, *J. Vac. Sci. Technol., A* 1987**, *5*** (2), 231-233.
95. B. Roldan Cuenya, *Acc. Chem. Res.* 2012, **46** (8), 1682–1691.
96. R. Reske, H. Mistry, F. Behafarid, B. Roldan Cuenya, P. Strasser, *J. Am. Chem. Soc.* 2014, **136** (19), 6978–6986.